

SI for 'Cavitation clusters in lipid systems – surface effects, local heating and streamer formation', Birkin *et al.*

Figure S1 shows a set of images and acoustic characteristics for water. Figure S1 (a) and (b) show images of an aged and fresh tip for the PLE deployed in the study respectively. The aged tip shows clear signs of erosion of the surface as a result of cavitation action. This is typical of PLE tips unless they have been carefully and regularly polished.

Figure S1 (c) and (d) show images (recorded with a stills camera) of the PLE tips operating in water under the same

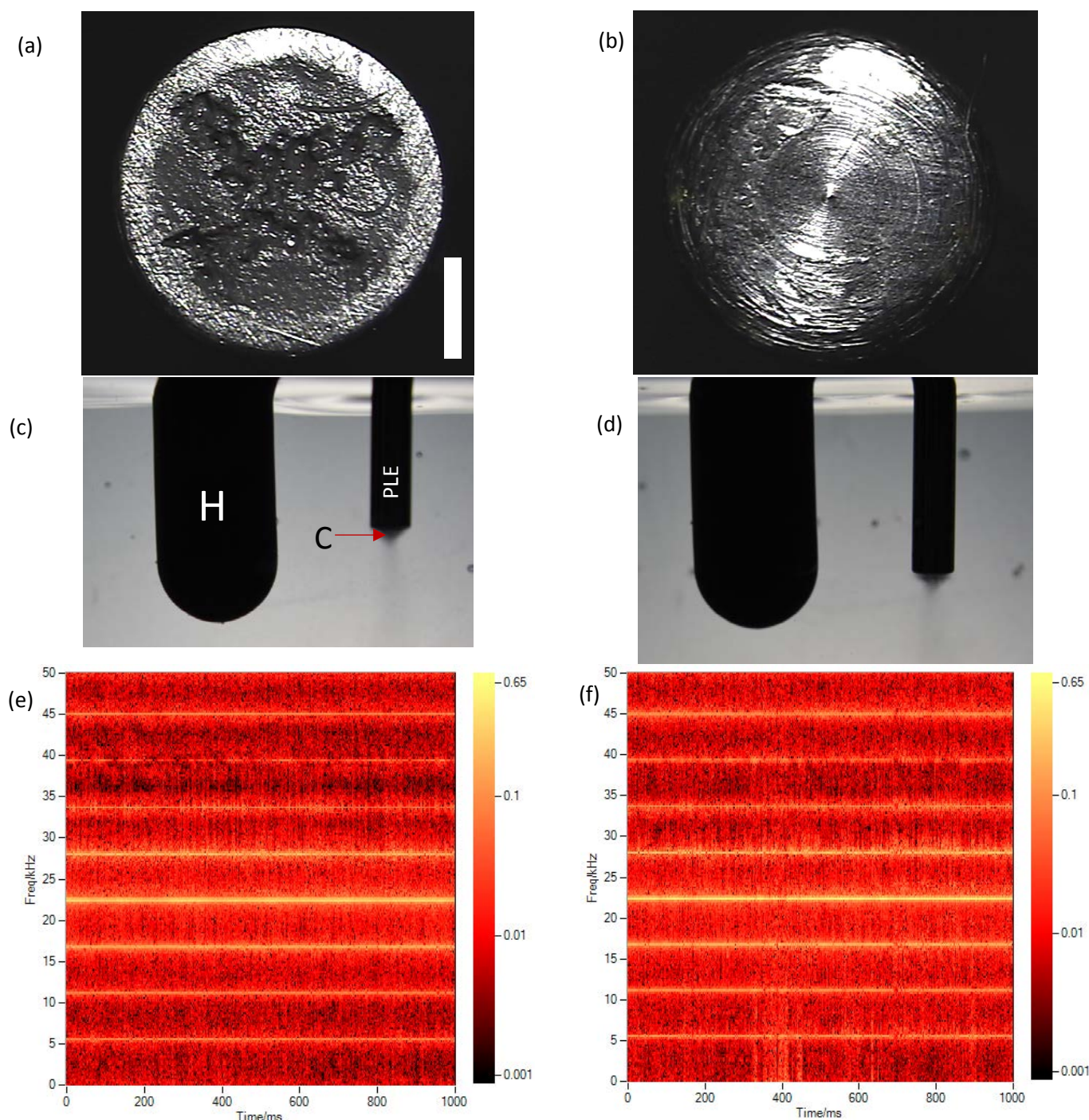


Figure S1. Image (a) and (b) show the aged and fresh tip respectively. Note the tips are 3.2 mm in diameter, scale bar = 1 mm in image (a). Image (c) and (d) show the cavitation plume generated by the operating PLE ($6 W_{rms}$, ~ 23 kHz) for the aged and fresh tip respectively. These images also show the cluster (C) and the hydrophone (H). Note, for scale, the hydrophone body is 9.5 mm in diameter. (e) and (f) show the results of the analysis of the acoustic emission recorded with a hydrophone (see (c)) for an aged and fresh tip respectively. The scale indicates the magnitude of the signal (in volts).

conditions. These images show the hydrophone positioned next to the PLE and the generation of the cluster (C) at the end of the tip (see image (c)). In order to show that this cluster was essentially the same despite the tip differences, the acoustic emission of the water system was captured and analysed using an FFT approach. Figure S1 (e) and (f) show the frequency components detected for the eroded (e) and fresh tip (f) plotted as a function of time. In this case

the emission characteristics show a signal for the PLE itself (centred on ~ 23 kHz) and a set of sub and ultra-harmonics (for example at $f/4$, $f/2$ and $3f/4$ for the subharmonics). These are characteristic of a $f/4$ periodicity of the cavitation cluster (where f is the fundamental drive frequency of the PLE). Note that in the case of water and under essentially identical conditions, the emission characteristics for the two PLE tips (eroded and fresh) are essentially the same. Thus, in water, the state of the surface of the PLE does not have as significant an effect on the dynamics of the cavitation cloud produced. This is in contrast to the oil system (see manuscript) where the state of the tip plays a key role in the cavitation cluster behaviour produced.

Figure S2 shows the analysis and an example image used to estimate the velocities of the flow in an oil/lipid system. Figure S2 (a) was used to estimate the fluid velocity under these conditions based on the slope of the distance time data. In this case, a velocity on the order of 11 m s^{-1} was estimated in the z direction.

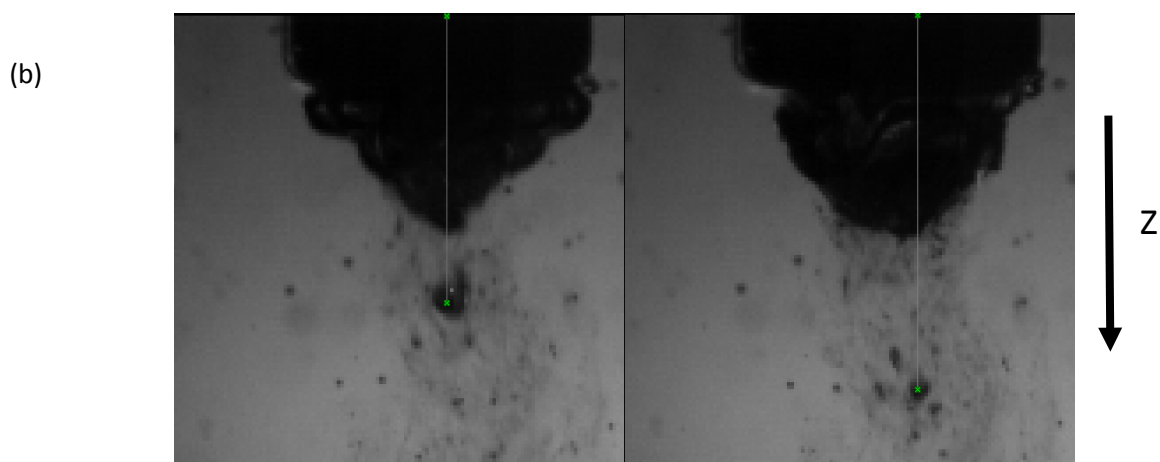
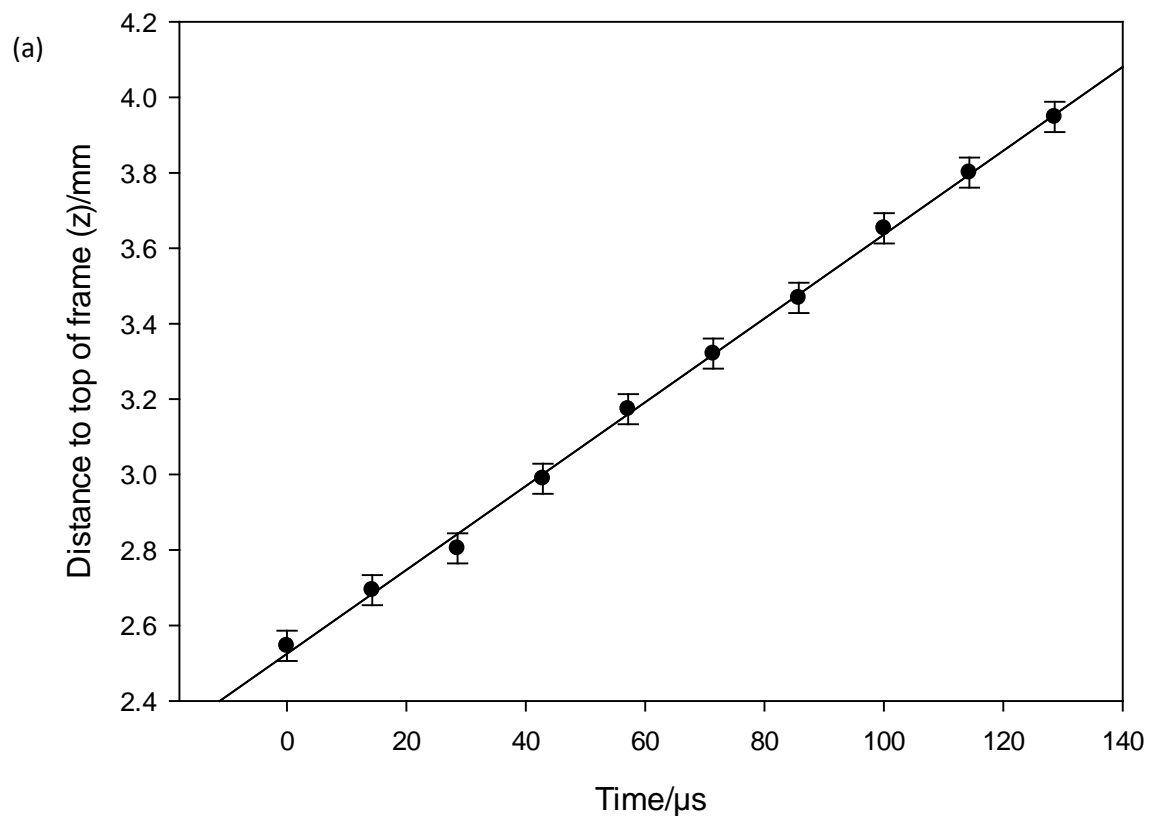


Figure S2. (a) plot showing the position of a gas bubble tracker as it moved away from the PLE operating in sunflower oil. The gradient of this plot enabled an estimate of the velocity (here 11.1 m s^{-1}) to be gathered in this region close to the PLE. The error bar represent an estimate of the uncertainty associated with the measurement of the position of the bubble in these images. (b) shows images of the PLE operating in oil. The measurement of the position of the tracked bubble is shown for completeness, here the bubble moved 0.92 mm in $85.7 \mu\text{s}$.

In order to characterise the tip performance further, and in the absence of a suitably calibrated hydrophone, the calorimetric output of an eroded tip was measured. Figure S3 (a) shows a schematic representation of the experimental setup used. Here a small volume (10 cm³) of the oil was placed in a vial. The temperature jump recorded for a set exposure to ultrasound from the PLE tip was then recorded. In order to ensure rapid mixing, and minimal heat loss, a stirrer bar was employed while the vial was insulated with ~ 4 mm of expanded polystyrene. The temperature jumps recorded using this method were found to be reproducible (see figure S3 (b) for example). Figure S4 shows the measured output of a tip as a function of the watts (rms) reported by the amplifier for a range of different drive amplitudes.

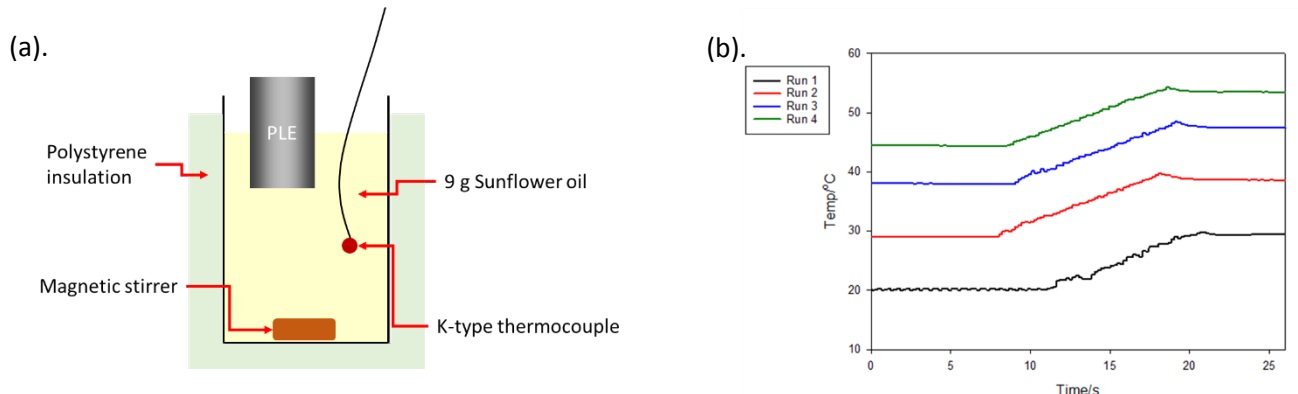


Figure S3 (a) Schematic representation of the cell used to measure the calorific effect of the eroded piston like emitter (PLE) in sunflower oil. **S3 (b)** Plot showing the temperature jump as a result of four repeat runs using the cell shown in figure S3 (a) and where a 10 s burst of ultrasound (28 W_{rms})

Note the red line is shown for guidance only. Although the temperature jumps were found to be reasonably reproducible, it was noted that a slow decline in temperature jump was observed as the baseline temperature of the oil increased.

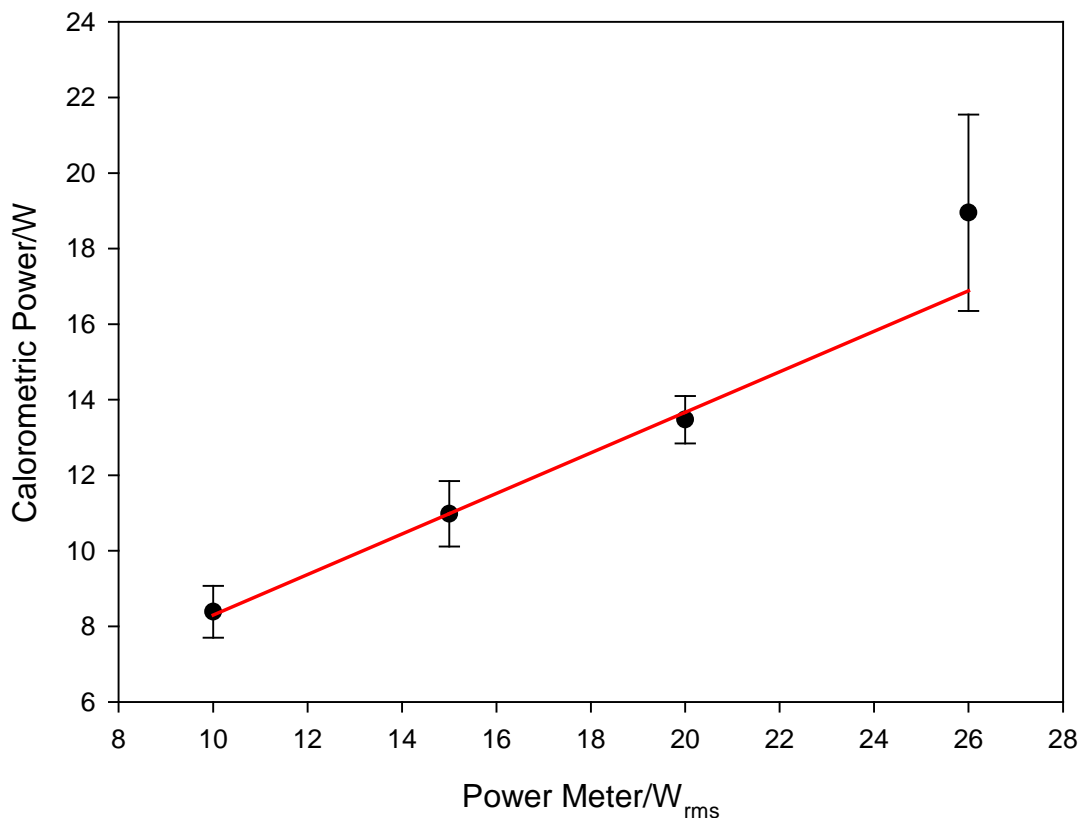


Figure S4. Plot showing the average (over 4 runs) (●) of the calorimetric heating rate recorded for an eroded tip as a function of the amplifier output in W_{rms}. The error bars correspond to the 95% confidence interval determined from the data obtained. Each run employed 10 cm³ of sunflower oil and an experimental setup depicted in figure 3 (a). Note the tip diameter was 3.2 mm.

The calorific output of the PLE was determined from the temperature jump, the mass of oil and the specific heat capacity of the sunflower of over this temperature range¹.

The physical properties of sunflower oil were also measured for reference. Figure S5a shows the shear stress plotted as a function of shear rate. This data indicates that the oil can be treated as a Newtonian fluid under the conditions stated.

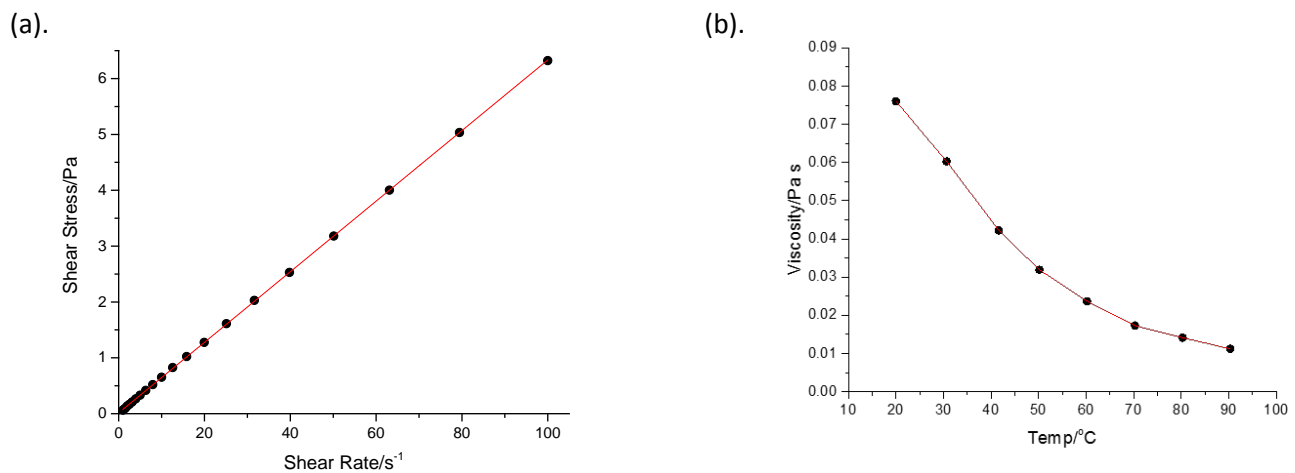


Figure S5 (a). Plot showing the shear stress as a function of shear rate for sunflower oil. The data was recorded at 25 °C. The gradient of this plot indicates a viscosity under these conditions of 0.0632 ± 0.0056 Pa s **(b).** Plot showing the viscosity of sun flower oil plotted as a function of temperature.

The viscosity of the oil, which are similar to literature values^{1,2}, is plotted as a function of temperature in figure S5b. Dynamic rheological data for sunflower oil has been reported by Yalcin *et al.*³.

The measurements reported in the main text were made under ‘steady state’ conditions (e.g. the piston like emitter had been initiated for a period of >1 second before measurements were made). Figure S6 shows examples of the laser scattering and the acoustic signature in a populated (b) and unpopulated (a) liquid. Figure S6b shows the case where bubbles were present from previous exposure to ultrasound and visible within the media. In this case scattering and an acoustic signature from the bubble activity within the cell occurs relatively rapidly.

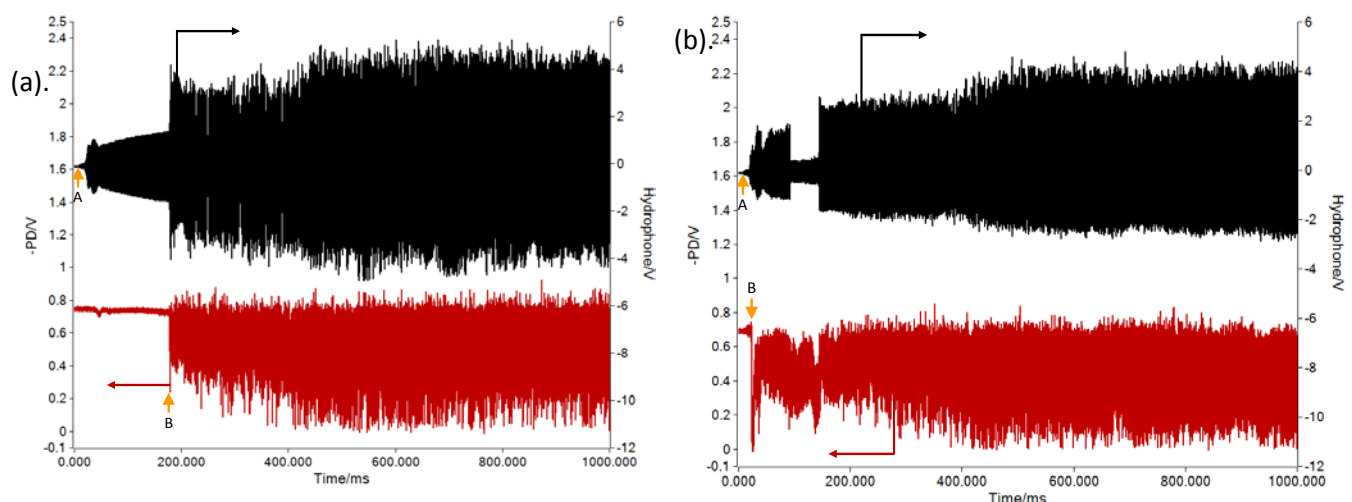


Figure S6 Plots showing the acoustic signature (—) measured in the cell and the associated laser scattering signal (—) as the PLE rings up. These signals were recorded simultaneously. The PLE was initiated at Time = 50 ms in both cases (see ‘A’). The onset of bubble activity at the tip of the PLE occurred at ‘B’. This was accompanied by transient scattering of the laser signal and an altered acoustic emission. This association with bubble activity was confirmed by high-speed images which indicated that this was required at the PLE tip before scattering (or the altered acoustic signature) was detected. In this experiment, the laser was position ~ 2.5 mm below the PLE. **(a)** corresponds to ‘bubble free’ where the oil had been left to stand undisturbed for ~2 hours, while **(b)** represents the case where the oil was populated with bubbles from prior ultrasonic exposure. The cell contained sunflower oil.

For the eroded tip in an oil containing bubbles, the ring up of the tip and the observation of bubble dynamics and in particular the cluster was relatively fast (~50 ms). However, if the oil was allowed to clear (see figure S6a) for a

significant period (up to 24 hours), the ring up process was longer but still < 200 ms under the conditions employed. In both cases the scattering and acoustic signature produced were associated with bubble activity in the system (particularly at the PLE tip where the cluster forms) which was confirmed by simultaneous high-speed imaging of the system.

The sound field generated in the system is also of interest. This is relevant to primary Bjerkness forces (BF) for example. Here bubble accumulation in both nodes and antinodes (depending on the resonant size of the bubbles with respect to the frequency of the sound field employed) is anticipated⁴. However, these primary BF were not observed to play a significant role in the experimental system deployed. This statement is supported by two factors; the lack of any banding observed in the cell and the calculated cell characteristics. In order to calculate the resonant nature of the cell, it is important to note that the boundary conditions, the materials employed in the cell and the complete dimensions of the cell that impact on the sound field (and the modes present) expected. If we consider the geometry of the cell employed (a rectangular cell measuring 60 mm x 60 mm x 130 mm) and the walls it is reasonable to consider two cases. In the first case, all boundaries are considered pressure release (for example a pressure node). While in the second case, the base of the cell is considered rigid (a pressure antinode). The normal modes for each case can then be calculated following standard acoustic texts⁵. Equation 1 and 2 show the natural frequencies (ν) predicted by such an approach respectively.

$$\nu_{n_x, n_y, n_z} = \left(\frac{c}{2}\right) \sqrt{\left\{\left(\frac{n_x}{L_x}\right)^2 + \left(\frac{n_y}{L_y}\right)^2 + \left(\frac{n_z}{L_z}\right)^2\right\}} \quad (1).$$

$$\nu_{n_x, n_y, n_z} = \left(\frac{c}{2}\right) \sqrt{\left\{\left(\frac{n_x}{L_x}\right)^2 + \left(\frac{n_y}{L_y}\right)^2 + \left(\frac{2n_z+1}{2L_z}\right)^2\right\}} \quad (2).$$

Where n_x , n_y and n_z represent the mode numbers (an integer value, 1, 2, 3...etc.), c the speed of sound in the medium and L_x , L_y and L_z the dimensions of the cell. Considering the dimensions of the cell and the speed of sound in the oil, it is possible to predict the normal modes for both models (see table 1).

nz	Equation (1). All pressure release./Hz	Equation (2). Rigid floor, pressure release walls./Hz
1	17852	18895
2	20266	21902
3	23750	25764
4	27907	30152

Table 1. Normal modes for the rectangular cavity (60 mm x 60 mm x 130 mm). Here $n_x = n_y = 1$ and $c = 1440$ m s⁻¹ (a typical value for a vegetable oil⁶).

None of the modes match the frequency used in the experiments (22.7 kHz) and hence are expected to be poorly driven. This, and the absence of any banding effects, suggest that these primary forces do not play a key role in the experiments reported. Other bubble effects (such as bubble/bubble interactions) cannot be ruled out and need further investigation.

- 1 O. O. Fasina and Z. Colley, *Int. J. Food Prop.*, 2008, **11**, 738–746.
- 2 J. Kim, D. N. Kim, S. H. Lee, S. H. Yoo and S. Lee, *Food Chem.*, 2010, **118**, 398–402.
- 3 H. Yalcin, O. S. Toker and M. Dogan, *J. Oleo Sci.*, 2012, **61**, 181–187.
- 4 T. G. Leighton, *The Acoustic Bubble*, Academic Press, London, 1994.
- 5 L. E. Kinsler, A. R. Frey, A. B. Coppens and J. V Sanders, *Fundamentals of Acoustics*, John Wiley & Sons, New York, 1982.

6 G. W. C. Kaye and T. H. Laby, *Tables of Physical and Chemical Constants and some Mathematical Functions*, Longmans, Green and Co, London, 12th edn., 1959.